



HAL
open science

A new modeling approach of myxococcus xanthus bacteria using polarity-based reversals

Hélène Bloch, Vincent Calvez, Benoît Gaudeul, Loïc Gouarin, Aline Lefebvre-Lepot, Tam Mignot, Michèle Romanos, Jean-Baptiste Saulnier

► To cite this version:

Hélène Bloch, Vincent Calvez, Benoît Gaudeul, Loïc Gouarin, Aline Lefebvre-Lepot, et al.. A new modeling approach of myxococcus xanthus bacteria using polarity-based reversals. CEMRACS 2022, Jul 2022, Marseille, France. <https://doi.org/10.1051/proc/202477025> . hal-04102694v2

HAL Id: hal-04102694

<https://hal.science/hal-04102694v2>

Submitted on 30 May 2024

HAL is a multi-disciplinary open access archive for the deposit and dissemination of scientific research documents, whether they are published or not. The documents may come from teaching and research institutions in France or abroad, or from public or private research centers.

L'archive ouverte pluridisciplinaire **HAL**, est destinée au dépôt et à la diffusion de documents scientifiques de niveau recherche, publiés ou non, émanant des établissements d'enseignement et de recherche français ou étrangers, des laboratoires publics ou privés.

A NEW MODELING APPROACH OF *MYXOCOCCUS XANTHUS* BACTERIA USING POLARITY-BASED REVERSALS *

HÉLÈNE BLOCH¹, VINCENT CALVEZ², BENOÎT GAUDEUL³, LOÏC GOUARIN¹, ALINE LEFEBVRE-LEPOT¹, TAM MIGNOT⁴, MICHÈLE ROMANOS² AND JEAN-BAPTISTE SAULNIER⁴

Abstract. The aim of this paper is to model the collective behavior of *Myxococcus xanthus* bacteria to better understand the emerging patterns at the level of the colony. We use image analysis and data treatment on experimental data of *Myxococcus xanthus* bacteria. We develop two models whose main novelty is the polarity-based reversals. The first model is based on contact dynamics approach and the second one is inspired by a molecular dynamics approach. We compare the two models and we show numerical simulations in 2D. The mathematical and biological aspects of each model are discussed.

Résumé. L'objectif de cet article est de modéliser le comportement collectif de la bactérie *Myxococcus xanthus* afin de comprendre les motifs émergents à l'échelle de la colonie. Nous utilisons l'analyse d'images et le traitement de données sur des données expérimentales de bactéries *Myxococcus xanthus*. Nous développons deux modèles dont la nouveauté est les inversions de polarité des bactéries. Le premier modèle est basé sur une approche de dynamique des contacts et le second s'inspire d'une approche de dynamique moléculaire. Nous comparons les deux modèles et nous montrons des simulations numériques en 2D. Les aspects mathématiques et biologiques de chaque modèle sont discutés.

1. INTRODUCTION

The observation of collective motion in various life forms reveals fascinating phenomena, where diverse movements contribute to the emergence of collective behaviors.

From flocking birds [29, 30] and schooling fish [27], to coordinated movements of ants and bees [28], coordinated behavior among individuals is a common feature in many systems. In this paper, we will focus on one particular system in which collective motion has been extensively studied: the bacterium *Myxococcus xanthus* (*M. xanthus*). It is known for its ability to exhibit collective behaviors such as swarming behavior, rippling, aggregation, and others. By investigating the mechanisms underlying these behaviors, we aim to gain a deeper understanding of the principles governing collective motion in this model organism and how they may be relevant to other systems.

* This work was supported by the European Research Council under Grant Agreement No 865711 and the French National Research Agency (ANR) through Grant ANR18-CE46-0005 (project RheoSUNN)

¹ CMAP, CNRS, Ecole Polytechnique, I.P. Paris, 91128 Palaiseau, France

² Institut Camille Jordan, Université Claude Bernard, Lyon, 69100, France

³ Université Paris-Saclay, CNRS, Laboratoire de mathématiques d'Orsay, 91405, Orsay, France

⁴ Laboratoire de chimie bactérienne, 13009 Marseille, France

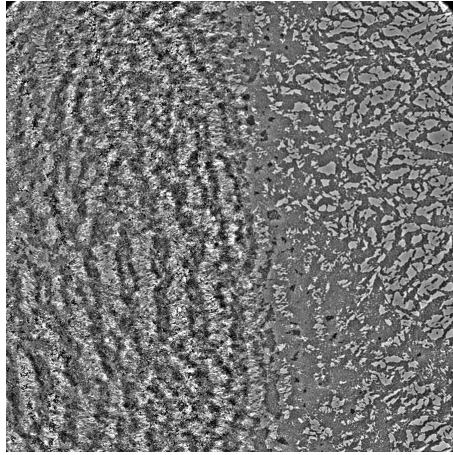


FIGURE 1. Frame taken from live movies of bacteria with 20 \times magnitude objective. Left: rippling (wave formation), right: swarming.

M. xanthus is commonly found in soil and measures a few micrometers. This bacterium is social, it interacts with its neighbors to form groups that synchronize their movements. In that case, macroscopic patterns such as rippling and swarming can be observed. Although, it is also able to move by its own means, this property is called *motility*.

Consider Fig. 1. The left part shows *rippling*. It is a periodic and synchronous wave that correspond to thousands of cells self-organizing into bands of traveling waves. In each band, the cells are highly aligned [24]. The right part of Fig. 1 shows *swarming*. It can take several forms. When bacteria explore new areas, they establish groups that move as a single organism, and in this case, the patterns formed by these groups change over time. After exploration, the colony begins to create a static pattern in which the cells follow specific roads. To move, these cells are equipped with a motor called the *adventurous machinery*, which allows bacteria to propel forward and move independently [18, 19].

Movements in groups are dictated by *social motility* and is mediated by the *type IV pili* (singular: *pilus* apparatus). A type IV pilus is a growth of the bacterium that can elongate, anchor to the substrate or to other cells, and retract, allowing the bacterium to move forward [15]. These machineries are localized and assembled at an extremity of the bacterium. These machineries can relocate at the opposite cell pole. When this happens, the bacterium rapidly changes direction of movement. This phenomenon is called a *reversal*. Mutants (genetically engineered bacteria) unable to reverse do not experience rippling and produce different patterns of swarming [12, 26]. This suggests that reversals play an important role in the formation of rippling patterns.

Cells can also secrete exopolysaccharide (EPS) proteins on the surface. After some time, this secretion forms a network. Pili can attach themselves to this network [15].

This paper is dedicated to the development, implementation and simulation of particle-based models which can reproduce and explain swarming and rippling patterns. To simulate rippling waves, the implementation of a refractory period (period of time during which the cell cannot reverse) seems to be crucial [4, 6, 16]. It is coupled with a sigmoid function dependent on a hypothetical signal that triggers the reversals. Biologically, this refractory period consists in the relocation time of a protein working for the reversal machinery [5]. In this case, global alignment is also required, and 1D models [4, 6, 16] are sufficient to show the emergence of rippling waves.

The complexity of modeling increases to reproduce swarming patterns. First, cells are not aligned, thus a 2D model is necessary. Second, a contact mechanism between cells to avoid overlap is required to see the emergence of groups of cells moving as a single organism. Furthermore, Balagam and Igoshin [1] show that an additional

mechanism called *slime trails following* allows to replicate patterns close to what can be observed experimentally. However, the paper does not investigate the dynamics of reversals and the authors use a constant refractory period, which is not observed in experiments [5]. We aim to build upon the model proposed by [1] and to extend it to explore diverse reversal triggering mechanisms. We adopt two approaches: the first one is based on contact dynamics and the second one is inspired by molecular dynamics. In both approaches, the polarity-based reversal mechanism stands out as a novel aspect, derived from analyzing experimental data. The main difference between the two approaches lies in the modeling of cell-cell dynamics. In the molecular dynamics-like approach, external forces are taken as functions of the distances between bacteria and are chosen to avoid cell overlap. In the contact dynamics approach, intercellular forces are unknowns of the problem.

The outline of the paper is as follows: in Sect. 2, we present the image and data analysis of experimental data on *M. xanthus*. In Sect. 3, we introduce the two mathematical models, based on the molecular dynamics approach and the contact dynamics approach. Section 4 details the implementation of the different models. Section 5 shows the numerical models obtained with these models. Finally, in Sect. 6 we discuss our results and their relevance to pattern formation in colonies of bacteria.

2. DATA ANALYSIS

In this section, we present the analysis of some experimental data on *M. xanthus* bacteria, namely the velocity and reversal times of the bacteria. We show some data acquisition techniques (image analysis and processing) as well as the result of data treatment and analysis, which will be the main pillars for the modeling of *M. xanthus* behavior, and for parameters calibration in the mathematical models.

2.1. Data acquisition and processing

To study the emergence of swarming patterns, we acquired data from the Laboratoire de Chimie Bactérienne (Marseille, France). These data consist in live segmented movies of a colony of *M. xanthus* bacteria containing roughly 1 000 bacteria in the frame of the camera. Figure 2 showcases the segmentation process. Figure 2a is a zoom of Fig. 1 in the swarming part, on the right of the image.

The variations of the light through different media allow to obtain an image with a phase contrast microscope (Fig. 2a). Segmentation (Fig. 2b) is the process by which each pixel in each image of the movie (corresponding to a time frame in our case) is assigned a label. Image segmentation of bacteria movies allows us to detect the body of each bacterium, and to separate it from the background (the medium). This process gives access to the position of each bacterium at each time frame. Each bacterium is represented by a sequence of points positioned along the body axis of the bacterium. In our case we extract nine points per bacterium, see Fig. 2c. Several algorithms for image segmentation exist, we chose the recently developed algorithm MiSiC [22] which has already given good results in the segmentation of colonies of bacteria.

It is worth noting that the segmentation process is not perfect. Common errors can occur, such as the merging of two bacteria, or defects in the process leading to a bacterium not being segmented. These defects motivate the work in Sect. 2.4. However, due to time constraints, only data directly obtained from the process presented here were used.

2.2. Analysis of bacteria velocity

As the bacteria are able to travel alone, form groups, and travel in packs, we investigated whether the bacteria's velocity depends on the size of the group. With the segmented data at hand, we divided the bacteria into three groups: isolated bacteria, bacteria traveling in packs of two to four bacteria and bacteria traveling in swarms (very large groups moving in the same direction). We tracked each bacterium in each subgroup (in total 5 bacteria were analyzed in each subgroup type). We observed that bacteria with one or more neighbors move on average faster in the medium than isolated ones, see Fig. 3. This suggests that group size affects bacteria's velocity.

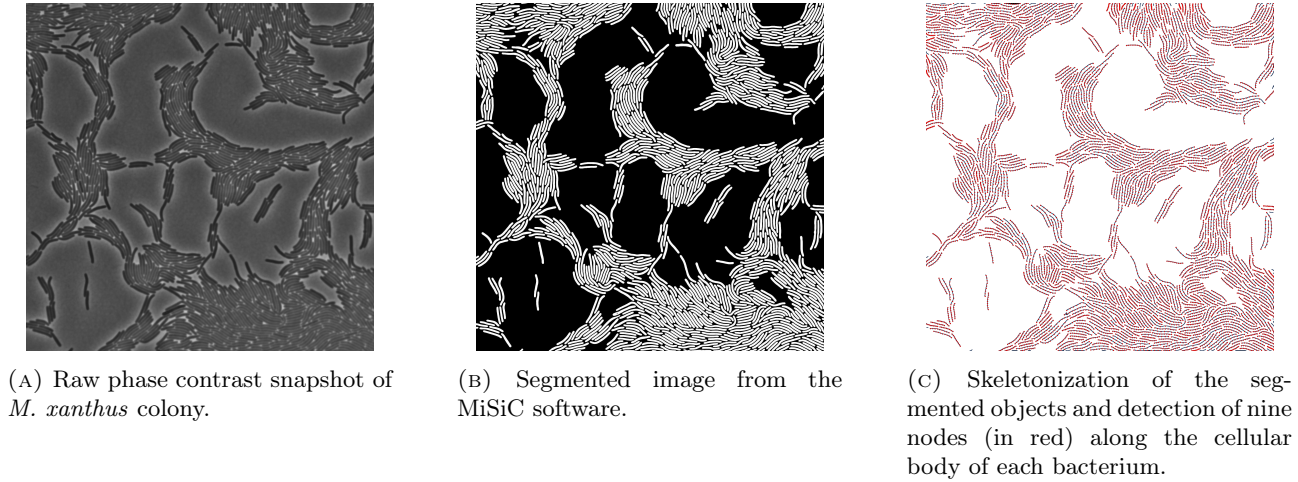


FIGURE 2. The different steps of the segmentation process for the same image. The images are obtained using a $100\times$ magnification objective.

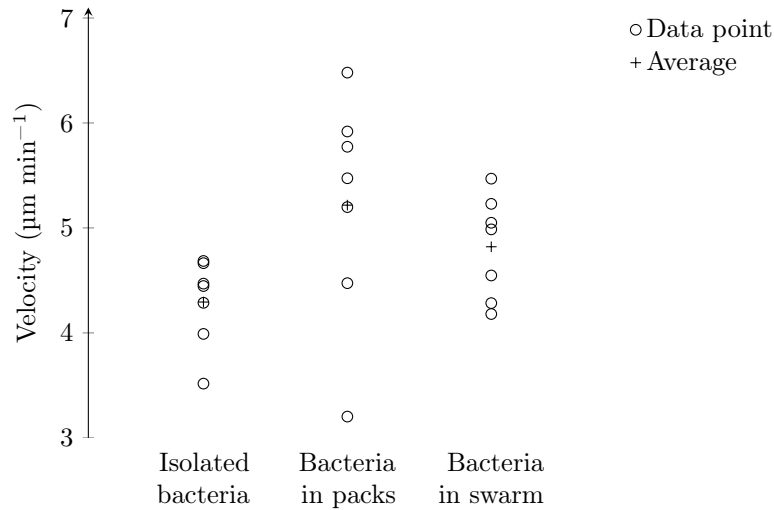
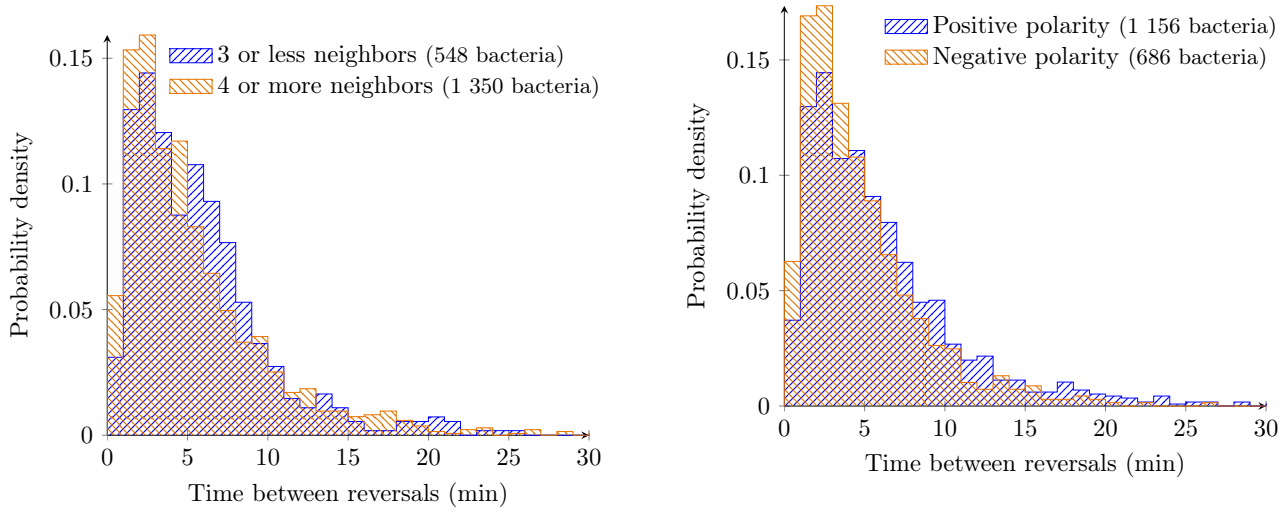


FIGURE 3. Bacteria's velocity depending on group size in three subgroups: isolated bacteria, bacteria in packs (groups of two to four bacteria), and bacteria in swarms.

2.3. Analysis of bacteria reversal frequency

When the tracking is consistent for a sufficiently long time, several reversal events can be observed. We analyzed the reversal frequency of a given bacterium in a swarm by computing the time between two reversals. This analysis revealed a distinctive distribution of these times, bacteria had 3 min to 3.5 min between each reversal event, see Figure 4a. Long times between two reversals can be underestimated because of segmentation and tracking errors, as well as the size of the field captured, and the duration of the movie. We then searched if these reversal frequencies were directly correlated with either the local density or the local mean polarity. For a given cell, the local density is defined as the number of neighbors in contact with the bacterium. The local



(A) Density histogram of the time between reversals for categories based on the number of neighbors at reversal.

(B) Density histogram of the time between reversals for categories based on the relative direction of neighbors at reversal.

FIGURE 4. Impact of the neighbors on the time between reversal.

mean polarity is defined as:

$$\bar{\Theta}(i) = \begin{cases} \frac{1}{N_{c,i}} \sum_{j=1}^{N_{c,i}} \frac{\mathbf{v}_i \cdot \mathbf{v}_j}{\|\mathbf{v}_i\| \|\mathbf{v}_j\|} & \text{if } N_{c,i} \geq 1, \\ 1 & \text{if } N_{c,i} = 0, \end{cases} \quad (1)$$

where i is the considered bacterium and $N_{c,i}$ is the number of cells in contact with the bacterium i . With a slight abuse of notation \mathbf{v}_i and \mathbf{v}_j are the average velocities of the nine points of bacterium i and of its j -th neighbor, respectively. We note here that two (or more) bacteria are *in contact* or *neighbors* if the distance between the center of one of the nine points where the velocity is measured is smaller than a certain threshold : 1 μm .

We compared the distribution of time between reversals for a low density (resp. negative polarity) of bacteria and for a high density (resp. positive polarity). In this case, we cannot divide the analysis into three categories as in Sect. 2.2, primarily because there are too few isolated bacteria to obtain sufficient reversal events and generate robust statistics for such a category. A bilateral Kolmogorov-Smirnov test showed that there is no link between the local density and the frequency of reversals ($p_{\text{value}} = 0.096$, see Fig. 4a). It revealed on the other hand that more frequent reversals might be linked to (or triggered by) a bacterium facing groups of opposite orientations ($p_{\text{value}} = 4.61e - 6$, see Fig. 4b), as we obtain a significantly lower mean of times between reversals for bacteria with negative polarity.

2.4. Trajectory smoothing

Experimental data on *M. xanthus* seems to suggest that reversals occur at rest, that is, the velocity of bacteria decreases before they stop. However, due to the discrete nature of the measurement process, computation of the velocity using the traditional two point approximation formula gives poor results. Indeed, we can measure a correlation coefficient lower than 0.5 (moderate to weak relation) between two consecutive time steps, even for trajectories which seem smooth enough to the naked eye. Moreover, during the segmentation process, incorrect merges of two bacteria might occur, leading to artificial spikes in the position of the bacterium's center of mass and tail or head. These spikes can corrupt the analysis of a dataset.

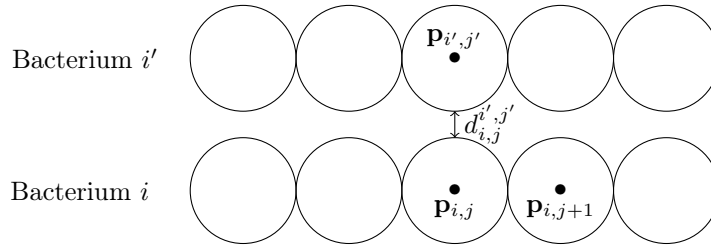


FIGURE 5. Notations for contacts.

To deal with these issues, we explored a smoothing of the trajectory based on an optimization problem. Due to the non smooth nature of the velocity near reversals, classical smoothing techniques should not be used, as they would hinder the precision of the measurements near reversals. The variable parametrizes a set of continuous and piecewise polynomial trajectories. The cost function is related to the L^2 distance between the tracking measurements and the smoothed trajectory at the time of these measurements. Dealing with the rare but large segmentation errors is done using a smooth minimum to reduce the cost they entail.

Our preliminary results (not shown here) are very promising but are outside the scope of this paper. These results suggest that using extrapolation on the smoothed trajectory could help stitch together parts of the trajectory provided by the current methodology and thus yield longer tracking time. This in turn could reduce the tracking errors which might have occurred during analysis of bacteria reversal frequency (Sect. 2.3).

3. MATHEMATICAL MODELING OF COLLECTIVE MOVEMENT OF *M. XANTHUS*

3.1. Modeling of bacteria

Inspired by [1], we model a bacterium as a string of disks moving on a plane. The disks forming a cell stay permanently in contact, either point-wise or with a fixed overlap. We call the centers of these disks *nodes*. As discussed in the introduction, a model in dimension at least two is required. In our experimental data, cells do not overlap, therefore, a 3D model is not necessary.

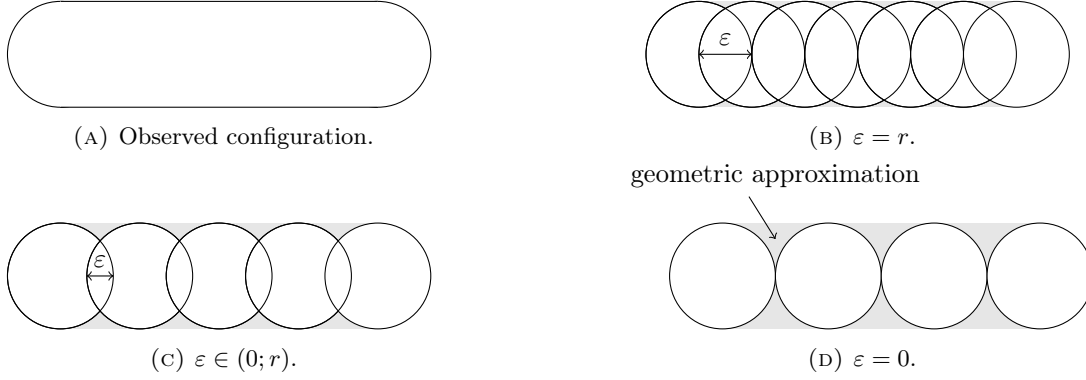
Let us write N the number of disks in a bacterium and r their radius. For the sake of simplicity, we assume that all disks have the same radius, even for two different bacteria.

We present a model that is continuous in time and space, the discretization of this system will be discussed in Sect. 4.2.

Let us consider M bacteria. For $i \in \llbracket 1, M \rrbracket$ and $j \in \llbracket 1, N \rrbracket$, let us write $\mathbf{p}_{i,j}$ the position of the center of the j -th disk of the bacterium i . For $i' \in \llbracket 1, M \rrbracket$ and $j' \in \llbracket 1, N \rrbracket$, we denote by $d_{i,j}^{i',j'} = \|\mathbf{p}_{i,j} - \mathbf{p}_{i',j'}\| - 2r$ the signed distance between the disk j in the bacterium i and the disk j' in the bacterium i' . Bacteria i and i' can be different. Two bacteria should not overlap, i.e., $d_{i,j}^{i',j'} \geq 0$ for two disks that are not consecutive in a bacterium (see Fig. 5). Furthermore, we impose $d_{i,j}^{i,j+1} \leq 0$ so two disks in a bacterium stay in contact.

M. xanthus is rod-shaped, that is it resembles Fig. 6a. Our modeling choice does not include this geometry directly. To obtain a closer version of the rod shape, we can allow two consecutive disks to overlap. The condition $d_{i,j}^{i,j+1} = 0$ is replaced by $d_{i,j}^{i,j+1} = -\varepsilon$ with $0 \leq \varepsilon \leq r$. With $\varepsilon = 0$, we recover the initial case (Fig. 6d). On the other hand, $\varepsilon = r$ leads to the configuration represented by Fig. 6b, but prevents the bacterium to bend. Figure 6c shows a bacterium with $\varepsilon \in (0, r)$. The cell can still bend, which is closer to the physical behavior of a bacterium.

Swarming patterns are characterized by groups of cells that move in packs with minimal superposition. To replicate such patterns in our simulations, a contact mechanism between the cells is mandatory. Formally, the positions $\mathbf{p}_{i,j}$, $i \in \llbracket 1, M \rrbracket$, $j \in \llbracket 1, N \rrbracket$ are assumed to be solutions of the following *ordinary differential*


 FIGURE 6. Modeled bacteria with different values of ε .

equation (ODE)

$$\frac{d}{dt} \mathbf{p}_{i,j} = \mathbf{v}_{\text{base},i,j} + \sum_{(i',j') \text{ such that } d_{i,j}^{i',j'} \leq r_c} \mathbf{v}_{c_{i,j}^{i',j'}} + \mathbf{v}_{e_{i,j}}, \quad (2)$$

where the cut-off radius r_c is explained in Sect. 4.2.1. The velocity $\mathbf{v}_{\text{base},i,j}$ represents the natural motion of a bacterium. It is the velocity a bacterium “wants” to have, without taking the presence of other bacteria into account. Choices for $\mathbf{v}_{\text{base},i,j}$ are discussed in Sect. 3.2. The velocity denoted by $\mathbf{v}_{c_{i,j}^{i',j'}}$ is a *contact velocity-correcting term* such that disks are subject to the conditions $d_{i,j}^{i',j'+1} = -\varepsilon$ for two consecutive disks in a bacterium and $d_{i,j}^{i',j'} \geq 0$ for other disks. Several choices are discussed in Sect. 3.3. Finally, $\mathbf{v}_{e_{i,j}}$ represents the *external velocity-correcting term* imposed on disk j in the bacterium i . It can be written as the sum of correcting-terms imposed by the disk j' on the bacterium i' and by the external medium where bacteria are moving. Then we have:

$$\mathbf{v}_{e_{i,j}} = \sum_{(i',j') \text{ such that } d_{i,j}^{i',j'} \leq r_c} \mathbf{v}_{e_{i,j}^{i',j'}} + \mathbf{v}_{e_{i,j}}^{\text{EPS}}.$$

We discuss the use of these velocity-correcting terms to model the rigidity of a bacterium in Sect. 3.5 and the modeling of type IV pili in Sect. 3.6. The cut-off radius r_c is explained in Sect. 4.2.1.

3.2. Natural motion of a bacterium

To describe the motion of an isolated bacterium i , we developed and implemented four models. All of them rely on a parameter v representing the norm of the speed of the bacterium which can be fixed using the analysis done in Sect. 2.2. We also introduce the vectors $\mathbf{e}_{i,j}^- = \frac{\mathbf{p}_{i,j-1} - \mathbf{p}_{i,j}}{\|\mathbf{p}_{i,j-1} - \mathbf{p}_{i,j}\|}$ and $\mathbf{e}_{i,j}^+ = \frac{\mathbf{p}_{i,j+1} - \mathbf{p}_{i,j}}{\|\mathbf{p}_{i,j+1} - \mathbf{p}_{i,j}\|}$. See Fig. 8 for a more visual definition, and let us notice that $\mathbf{e}_{i,j+1}^- = -\mathbf{e}_{i,j}^+$.

In the first model, we assume that the bacterium is a rigid non-rotating body so that we have, for all nodes j , $\mathbf{v}_{\text{base},i,j} = \mathbf{v}_{\text{base},i,1}$. We also set $\mathbf{v}_{\text{base},i,1} = v\mathbf{e}_{i,2}^-$. We named this model *parallel* due to the orientation of the velocities.

In the second model, we also want the speed to be v , however, we assume that only the head (the first disk in the string) participates in the motion of the bacterium thus $\mathbf{v}_{\text{base},i,1} = Nv\mathbf{e}_{i,2}^-$ and $\mathbf{v}_{\text{base},i,j} = \mathbf{0}$ for $j \in \llbracket 2, N \rrbracket$. This model could be accurate for a pili-driven motility, we will refer to it as *towed*.

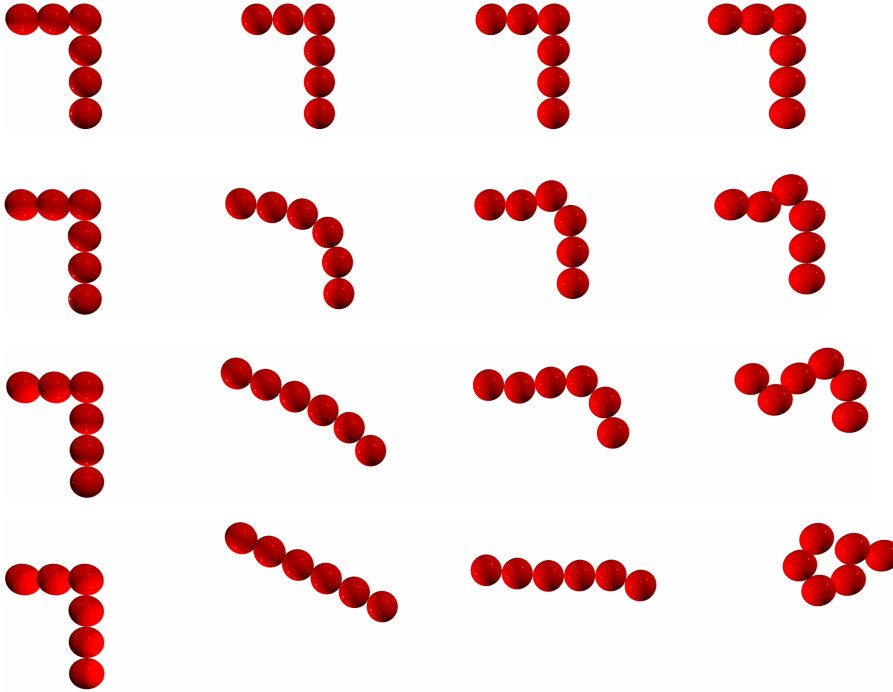


FIGURE 7. Trajectory of non-straight bacterium moving to the left. From top to bottom with parallel, towed, pulled, and pushed mobility. From left to right at adimensional times 0, 5, 15, 30.

The last two models are somewhat similar in their conception. They are respectively called *pulled* and *pushed*. For both of them we have $\mathbf{v}_{\text{base } i, 1} = v\mathbf{e}_{i, 2}^-$ and $\mathbf{v}_{\text{base } i, N} = v\mathbf{e}_{i, N}^-$ the difference lies in the inner nodes:

$$\mathbf{v}_{\text{base } i, j} = \begin{cases} v\mathbf{e}_{i, j}^- & \text{pulled model,} \\ -v\mathbf{e}_{i, j}^+ & \text{pushed model,} \end{cases}$$

so that as their names indicate the nodes are either pulled by the one in front of them or pushed by the one behind them. A convex combination of these models could be used to model the autonomous motility of *M. xanthus*.

As one can notice from Fig. 7 the pushed model does not yield realistic results, but we include it for symmetry purposes and to allow linear combinations of the models. We discuss this idea in Sect. 6. We note here that the 3D visual effect of disks in Fig. 7 is only a choice of visualization. All computations are performed on a plane.

3.3. Treatment of contacts

To complete the description of *M. xanthus*, we still need to model the contacts between bacteria. We explored two different methods.

In Sect. 3.3.1, we use a contact dynamics approach where the velocity-correcting terms $\mathbf{v}_{c_{i, j}^{i', j'}}$ are unknowns of the problems. They are deduced from Lagrange multipliers associated to the constraint on $d_{i, j}^{i', j'}$. A second method is discussed in Sect. 3.3.2. It is inspired by molecular dynamics, in the sense that the velocity-correcting terms $\mathbf{v}_{c_{i, j}^{i', j'}}$ are given by an explicitly computable formula such as Hook's law. Nevertheless, the velocity-correcting terms can be stiff, which can be challenging to treat numerically.

These two methods enable us to investigate the effect of different contact models on the emergence and stability of swarming patterns.

3.3.1. Contact dynamics approach

This method has been developed in [10, 11, 20, 21] to study the motion of rigid mechanical particles. In this method, the contact velocity-correcting terms are not functions of the distance. They are proportional to the Lagrange multiplier associated to the constraint on the distance. In the continuous model, if the initial condition does not satisfy the constraints, these velocities are no longer functions of the time but may include Dirac masses. The implicit scheme used to approximate them in Sect. 4.2 is still naturally well defined in most of these pathological conditions. For sake of readability we will not attempt to extend our continuous definition to these edge cases.

This method is typically used to impose a positive distance between two particles. In [7], it has been extended to particles that stay in contact. We shall consider two cases:

- if the two disks are consecutive in a bacterium, we impose $d_{i,j}^{i,j'} = -\varepsilon$ for $i \in \llbracket 1, M \rrbracket$, $j \in \llbracket 1, N \rrbracket$ and $j' = j - 1$ (if $j \neq 1$) or $j' = j + 1$ (if $j \neq N$);
- otherwise, we impose $d_{i,j}^{i',j'} \geq 0$ for $i, i' \in \llbracket 1, M \rrbracket$, $j, j' \in \llbracket 1, N \rrbracket$, and in the special case $i' = i$, then we have $j' \notin \llbracket j - 1, j + 1 \rrbracket$.

To stay in the framework of contacts dynamics, the first condition writes,

$$d_{i,j}^{i',j'} \geq -\varepsilon \text{ and } d_{i,j}^{i',j'} \leq -\varepsilon.$$

The implementation of this method is detailed in Sect. 4.1.1

3.3.2. Molecular dynamics-like approach

Unlike the model described in Sect. 3.3.1, the contact velocity-correcting terms have an explicit formulation. Even though the scales are quite different, this modeling relies heavily on a molecular dynamics approach [3]. A repulsive velocity-correcting is used to enforce the constraint that prevents the disks to overlap. We use the Hooke's law to impose $d_{i,j}^{i,j \pm 1} = -\varepsilon$ for two consecutive nodes and a quadratic velocity-correcting term to have $d_{i,j}^{i',j'} \geq 0$ for other nodes.

The Hooke's law to control the distance between disks. Enforcing a constant distance requires a velocity-correcting term that acts as a repulsive force if the nodes are too close, and as an attractive force if they are too far away. We model the contact velocity-correcting term as a spring with high stiffness between each consecutive node of a bacterium. This yields the following velocity-correcting term:

$$\mathbf{v}_{c_{i,j}}^{i,j+1} = k_s(d_{i,j}^{i,j+1} + \varepsilon)\mathbf{e}_{i,j}^+ \quad \text{and} \quad \mathbf{v}_{c_{i,j}}^{i,j-1} = k_s(d_{i,j}^{i,j-1} + \varepsilon)\mathbf{e}_{i,j}^-$$

where k_s is the stiffness constant of the springs.

Repulsion between disks. To avoid overlap between non-consecutive disks, we apply a repulsive velocity-correcting term between each disk j and another disk close enough j' . The same correction to the velocity is applied whether the two disks belong to the same bacterium or not, as long as they are not consecutive in a single bacterium ($j' \notin \llbracket j - 1, j + 1 \rrbracket$ if the two disks belong to the same bacterium). This repulsive term is quadratic to avoid too strong repulsion in case of a small overlap while preventing large overlaps. Formally, we set:

$$\mathbf{v}_{c_{i,j}}^{i',j'} = -k_r \left(\min \left(d_{i,j}^{i',j'}, 0 \right) \right)^2 \mathbf{e}_{i,j}^{i',j'},$$

where k_r is the repulsion coefficient of the repulsive velocity-correcting term and $\mathbf{e}_{i,j}^{i',j'}$ is the normalized vector pointing from the position $\mathbf{p}_{i,j}$ to the position $\mathbf{p}_{i',j'}$, $\mathbf{e}_{i,j}^{i',j'} = \frac{\mathbf{p}_{i',j'} - \mathbf{p}_{i,j}}{\|\mathbf{p}_{i',j'} - \mathbf{p}_{i,j}\|}$. The choice of a squared distance allows for C^1 regularity in the formulation of the velocity-correcting terms, while the minimum ensures that the

correction acts only for overlapping objects. We recall that the repulsive correction between a disk and both itself and its adjacent neighbors coming from the same chain of disks are set to 0.

3.4. Reversal mechanisms

We tested three different reversal mechanisms to understand how they can be linked to the swarming patterns. We first tested if it can emerge without any reversals. Then, based on biological data suggesting the presence of an internal clock governing the bacteria's reversal [5], we considered this possibility by conferring asynchronous reversal clocks to the bacteria colony. Upon reaching its intrinsic clock period, the bacterium reverses its body axis. Finally, as our data analysis (Sect. 2.3) revealed a link between the surrounding polarity of each bacterium and the reversal frequencies, we tested if this reversal mechanism can induce the swarming pattern. The bacterium i reverses its axis if it is facing more oppositely-directed bacteria than bacteria with the same direction as its own, i.e., if $\bar{\Theta}(i) < 0$, where the polarity $\bar{\Theta}$ is defined in Sect. 2.3. Our last model encompasses features from the other two. It is a stochastic model. Past a refractory time t_{ref} , we use a memoryless law whose parameter λ depends on the polarity. Formally between times t and $t + \Delta t$ the reversal probability of a bacterium i is $\lambda_i \Delta t + o(\Delta t)$. The term λ_i can be computed using the time since the last reversal of the bacterium $t_{c,i}$, the refractory time t_{ref} , a dimensionless parameter w representing the willingness to reverse, and the polarity $\bar{\Theta}(i)$ defined by Eq. (1) in Sect. 2.3.

$$\lambda_i = \begin{cases} 0 & \text{if } t_{c,i} < t_{\text{ref}}, \\ 1 - \exp\left(-w \frac{1 - \bar{\Theta}(i)}{2}\right) & \text{otherwise.} \end{cases}$$

3.5. Stiffness of a bacterium

The mathematical modeling of a bacterium as an ideal string of disks allows motions that are not observed in experiments, especially when bacteria bend. To tackle this issue, we use *external velocity-correcting terms* to model the stiffness of a cell. In this section, we consider a commonly used model [7, 8]. In Appendix A, we show that this model does not preserve the inter-center distances and thus required additional corrections for the contacts to be consistent with the framework presented in previous section. A second model, derived from a gradient-flow, is introduced to remedy this issue. Finally, we discuss the relative merits of each model.

The first model is given by angular springs and an action-reaction principle. Given a bacterium i and an inner disk $j \in \llbracket 2, N-1 \rrbracket$, we let $R = 2r - \varepsilon$ the distance between $\mathbf{p}_{i,j-1}$ and $\mathbf{p}_{i,j}$. As previously stated, this is also the distance between any two nodes and in particular, $\mathbf{p}_{i,j}$ and $\mathbf{p}_{i,j+1}$. We add the following corrections to the bacterium's velocity:

$$\begin{aligned} \mathbf{v}_{\mathbf{e}_{i,j-1}^{i,j}} &= -\frac{k}{R} (\mathbf{e}_{i,j}^+ - (\mathbf{e}_{i,j}^- \cdot \mathbf{e}_{i,j}^+) \mathbf{e}_{i,j}^-) && \text{on disk } j-1 \\ \mathbf{v}_{\mathbf{e}_{i,j+1}^{i,j}} &= -\frac{k}{R} (\mathbf{e}_{i,j}^- - (\mathbf{e}_{i,j}^- \cdot \mathbf{e}_{i,j}^+) \mathbf{e}_{i,j}^+) && \text{on disk } j+1 \\ \mathbf{v}_{\mathbf{e}_{i,j}^{i,j}} &= -\mathbf{v}_{\mathbf{e}_{i,j-1}^{i,j}} - \mathbf{v}_{\mathbf{e}_{i,j+1}^{i,j}} && \text{on disk } j, \end{aligned} \tag{3}$$

where k is a constant representing the stiffness of a bacterium. As shown in Fig. 8, the velocity-correcting terms $\mathbf{v}_{\mathbf{e}_{i,j-1}^{i,j}}$ and $\mathbf{v}_{\mathbf{e}_{i,j+1}^{i,j}}$ are orthogonal to $\mathbf{e}_{i,j}^-$ and $\mathbf{e}_{i,j}^+$ respectively. This is intuitively consistent to what one would expect from a stiffness model, however, since the correction on the middle node is not zero (to preserve the action-reaction principle), the inter-center distances are not preserved. See Appendix A for more details.

3.6. Type IV pili modeling

M. xanthus bacteria use type IV pili machinery located on their leading pole to move. These pili can elongate, anchor to EPS or to other bacteria, and retract to propel the cell forward [15]. Experiments with mutants lacking this machinery show a decrease in group size and coordinated motion [18, 31].

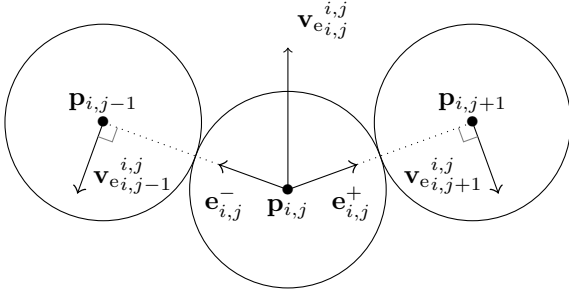


FIGURE 8. Notations and velocity-correcting terms at play with model Eq. (3) for bacterium i .

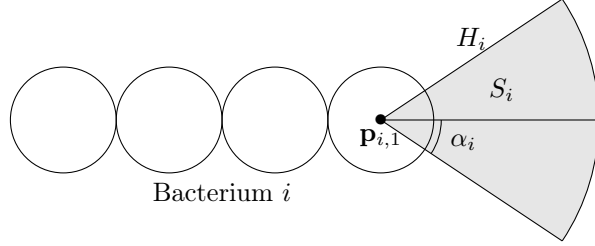


FIGURE 9. Notations used to define the pili search area.

In the following sections, we describe how we model the type IV pili mechanism. First we define the region reached by the pilus, then we model both the attraction with other bacteria and the EPS.

3.6.1. Pili search area

We suppose that *M. xanthus* can elongate its pili only in the forward direction. More precisely, the bacterium i can detect neighbors with an angle of view $2\alpha_i$, $\alpha_i \in [0, \frac{\pi}{2}]$, in front of it and a horizon $H_i > 2r$. Let us recall that $\mathbf{e}_{i,2}^-$ is the direction of the head so that the area of the plane viewed by the bacterium is formally given by:

$$S_i = \{ \mathbf{x} \in \mathbb{R}^2 \mid \exists l \in (0, H_i], \theta \in [-\alpha_i, \alpha_i], \mathbf{x} = \mathbf{p}_{i,1} + lQ(\theta)\mathbf{e}_{i,2}^- \},$$

where $Q(\theta) = \begin{pmatrix} \cos(\theta) & \sin(\theta) \\ -\sin(\theta) & \cos(\theta) \end{pmatrix}$ is the rotation matrix of angle θ . See Fig. 9 for a more visual definition of the notations.

3.6.2. Attraction with neighbors

Given that the pili are localized at the cell pole, we added a correction term for the velocity representing an attraction force on the head of each bacterium. This attraction term is defined as being in the direction of the head to the closest node of another bacterium in its field of view S_i . Let i' , ($i' \neq i$) and j' be the label of this other bacteria and node respectively. If the other bacteria are too far away, the velocity-correcting term for the attraction force is set to zero. Otherwise, the strength of this attraction is a function of the distance between the two bacteria, as illustrated by Fig. 10. This function is continuous, polynomial by part and equal to zero if the bacteria are in contact or too far away. It is given by the following formula:

$$\mathbf{v}_{\mathbf{e}_{i,1}^-}^{i',j'} = -k_a d^{\text{norm}} (d^{\text{norm}} - 1) (4 + (d^{\text{norm}} - 1/2)(8 - 16d^{\text{norm}})) \mathbf{e}_{i,1}^{i',j'},$$

where d^{norm} , the normalized distance is a number between 0 and 1. It can be obtained from the distance with the closest neighbor $\mathbf{p}_{i',j'}$ using $d^{\text{norm}} = \min \left(\max \left(\frac{d_{i,1}^{i',j'}}{H_i - 2r}, 0 \right), 1 \right)$. Notice that we do not enforce the principle of action-reaction and leave the attracting node unchanged. This models the stronger bound with the substrate in the middle of a bacterium.

3.6.3. Slime trail following

In this section we focus on the modeling of the EPS using a slime trail following, as Balagam and Igoshin [1]. In this model, each bacterium deposits a certain amount of EPS during its displacement which evaporates with a rate λ . To avoid feedback-loops, the EPS is deposited by the tail node of the bacterium only. The velocity-correcting term induced by the EPS models a nematic alignment with the point of highest concentrations,

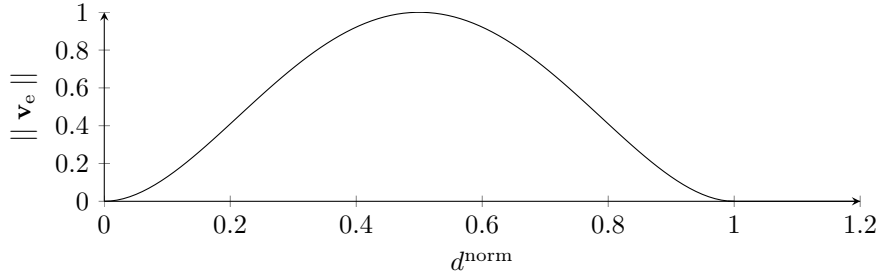


FIGURE 10. Attraction velocity-correcting term as a function of the distance between two bacteria.

provided it reaches a sufficient threshold. If the threshold is not met, the correcting term is set to zero. Else, the velocity-correcting term does not depend on the value of this concentration but only on the angle between the direction of the bacterium and the point of highest concentration.

Implementation details are provided in Sect. 4.2.2.

4. IMPLEMENTATION

4.1. Numerical schemes

We use a standard discretization in time, with a fixed time step Δt , and we write $t^n = n\Delta t$, with $n \in \mathbb{N}$. The external velocity-correcting terms are discretized explicitly, however the contact velocities terms are implemented implicitly for the contact dynamics approach and a Lie splitting [25] is used when the velocity-correcting terms have an explicit formula.

4.1.1. Numerical scheme for contact dynamics

As explained previously, with the contact dynamics approach, contact terms are unknowns of the problem, thus we need to treat them with an implicit scheme. Formally we set:

$$\mathbf{p}_{i,j}^{n+1} = \mathbf{p}_{i,j}^n + \Delta t \mathbf{v}_{\text{base}_{i,j}}^n + \Delta t \sum_{(i',j') \text{ such that } d_{i,j}^{i',j',n} \leq r_c} \mathbf{v}_{c_{i,j}}^{i',j',n+1} + \Delta t \sum_{(i',j') \text{ such that } d_{i,j}^{i',j',n} \leq r_c} \mathbf{v}_{e_{i,j}}^{i',j',n}, \quad (4)$$

where the superscript n (resp. $n+1$) indicates that the corresponding object is evaluated at time t^n (resp. t^{n+1}). The parameter r_c is a cut-off radius used for performance purposes. In fact, for particles far enough, the two velocity-correcting terms $\mathbf{v}_{c_{i,j}}^{i',j',n}$ and $\mathbf{v}_{e_{i,j}}^{i',j',n}$ are negligible in front of the other velocity-correcting terms, so they are set to 0. Let us notice that we do not discuss the external velocity-correcting terms applied by the external medium $\mathbf{v}_{e_{i,j}}^{\text{EPS}}$.

This model can be written as the resolution of a convex optimization problem under constraint at each time step:

$$\min_{\mathbf{v}^{n+1} \in K^{n+1}} J(\mathbf{v}^{n+1}), \quad (5)$$

with

- with a slight abuse of notation, $\mathbf{v}^{n+1} \in \mathbb{R}^{NM}$ refers to both the variable and the solution of this convex problem; it is a vector that contains the velocities of all nodes in all bacteria at time t^{n+1} ;
- $J(\mathbf{v}) = \frac{1}{2} \|\mathbf{v} - \mathbf{V}^{n+1}\|^2$, where \mathbf{V}^{n+1} is the *free flight velocity* given by $\mathbf{V}^{n+1} = \mathbf{v}_{\text{base}}^n + \mathbf{v}_e^n$, where $\mathbf{v}_e^n \in \mathbb{R}^{NM}$ is a vector that contains the resulting (or sum of) external velocity-correcting terms applied to all nodes in all bacteria.
- K^{n+1} is the set of admissible velocities; it is made of affine inequality constraints for each disk.

From [13], \mathbf{v}^{n+1} is the projection of \mathbf{V}^{n+1} on K^{n+1} . We then let:

$$\mathbf{p}_{i,j}^{n+1} = \mathbf{p}_{i,j}^n + \Delta t \mathbf{v}^{n+1}.$$

At each time step, an optimization problem has to be solved. Several methods exist in literature. In this work, we use a fixed-step projected gradient descent as a blackbox algorithm, also known as Uzawa method [17]. The convergence of this method was not studied and numerical parameters used can be found in Table 1.

Further details about the derivation of Eq. (5) can be found in [13]. This model is implemented in the code SCoPI developed at CMAP laboratory [14].

Solving a convex optimization problem at each time step is costly, thus we attempt to keep a large time step. Numerous algorithms based on iterative methods exist and which are not discussed here. To ensure convergence, we restrict the value of Δt with a rule of thumbs, such that a node is moved at most of 30% of its radius at each time step.

4.1.2. Numerical scheme for velocity-correcting terms with explicit formula

Since the contact forces can be stiff to ensure small penetrations, a small value of Δt should be used. Computing all the forces at each time step would be very costly, therefore a Lie splitting is implemented. Formally we let $\tilde{\mathbf{p}}_{i,j}^n$ encompass the velocities defined previously except for the contact corrections based on Hook's law: $\mathbf{v}_{c_{i,j}}^{i,j-1}$ and $\mathbf{v}_{c_{i,j}}^{i,j+1}$ which require a finer time step and the EPS which requires a grid search:

$$\tilde{\mathbf{p}}_{i,j}^n = \mathbf{p}_{i,j}^n + \Delta t \mathbf{v}_{\text{base}_{i,j}}^n + \Delta t \sum_{(i',j') \text{ such that } d_{i',j'}^{i',j',n} \leq r_c} \mathbf{v}_{e_{i,j}}^{i',j',n} + \Delta t \sum_{(i',j') \text{ such that } d_{i',j'}^{i',j',n} \leq r_c \text{ and } (i',j') \neq (i,j \pm 1)} \mathbf{v}_{c_{i,j}}^{i',j',n},$$

then compute:

$$\tilde{\mathbf{p}}_{i,j}^{n+\frac{k+1}{N_t}} = \tilde{\mathbf{p}}_{i,j}^{n+\frac{k}{N_t}} + \frac{\Delta t}{N_t} \left(\mathbf{v}_{c_{i,j}}^{i,j-1,n,k} + \mathbf{v}_{c_{i,j}}^{i,j+1,n,k} \right),$$

where N_t is a fixed number of subcycles and $k \in \llbracket 0, N_t - 1 \rrbracket$. Finally, we let:

$$\mathbf{p}_{i,j}^{n+1} = \tilde{\mathbf{p}}_{i,j}^{n+1} + \Delta t \mathbf{v}_{e_{i,j}}^{\text{EPS},n},$$

where $\mathbf{v}_{e_{i,j}}^{\text{EPS},n}$ is set to zero for $j \neq 1$ and will be detailed in Sect. 4.2.2.

If we were to chose k_r and k_s large and to add both contact forces in the Lie splitting, it could be seen as an approximate solution of the optimization problem presented above, however it comes from a different modeling approach.

4.2. Implementation

The two modeling approaches described previously were implemented in two different codes, each corresponding to one of the two methods described in Sect. 3.3 to treat inter-bacteria contacts.

The contact dynamics approach (Sect. 3.3.1) is implemented in the code SCoPI. This code is designed for the simulation of interacting particles. It is written in C++ and uses multithreaded libraries to be executed in a high performance computing (HPC) context. We implemented the string of disks model, as well as the different motions described in Sect. 3.2, the stiffness model (Sect. 3.5), the different reversion models (Sect. 3.4), and the attraction with neighbors model (Sect. 3.6.2). The simulations with SCoPI were performed in an infinite medium.

The method using velocity-correcting terms with an explicit formula (Sect. 3.3.2) was implemented in a code written in Python. The models implemented in SCoPI were also implemented in this code and the type IV pili model described in Sect. 3.6.3 was added. The simulations performed with the Python code were carried out in a periodic domain.

4.2.1. Detection of neighbors

We must detect the neighbors of all disks, either to build the matrix of constraints in the contact dynamics model, or to compute the corrections applied on the disk when these terms have an explicit formula. Several choices of implementation can be done. In SCoPI, a dynamic list is updated at each time step. In the Python code, we search for the K neighbors of each bacterium (so that each bacterium has exactly K neighbors), with K chosen large enough so that all bacteria in a given radius are considered as neighbors. We then use a cut-off radius r_c so that only cells inside this radius are considered as the bacterium's effective neighbors¹ with which velocity-correcting terms will be applied.

For performance reasons, both codes use kd-trees to determine the closest neighbors, such as the one implemented by the libraries nanoflann [2] or SciPy [?] spatial algorithms.

4.2.2. Implementation of the slime trail following

We now exhibit the details of the implementation of the slime trail following in the Python code. For the positions of the nodes we used a grid-less approach. Keeping this principle to deal with EPS deposits is overly costly since it would require to keep in memory the history of all bacteria. Therefore, we introduce a Cartesian grid $\Gamma = \Delta x \mathbb{Z}^2$. This grid can then either be truncated or stored sparsely. For any point $\mathbf{x} \in \Gamma$ we denote by $c(\mathbf{x})$ the amount of EPS present at this point.

At each time step, and for each bacterium, a normalized quantity 1 is added to $c(\mathbf{x}_i)$, where $\mathbf{x}_i \in \Gamma$ is the grid point closest to $\mathbf{p}_{i,N}$ the last node or tail of the bacterium. Once each bacterium has deposited EPS, the value on the grid c is multiplied by $\exp(-\lambda \Delta t)$ to account for the evaporation.

The slime trail impacts the trajectory of a bacterium i when it is present in sufficient quantity c_{\min} at a grid point in the cell's field of view S_i , where S_i was defined in Sect. 3.6. In this case, we let $\mathbf{x}_{\text{EPS},i} = \arg \max_{\mathbf{x} \in S_i \cap \Gamma} c(\mathbf{x})$ be the grid point with the highest value in S_i , $\mathbf{e}_{\text{EPS},i} = \frac{\mathbf{x}_{\text{EPS},i} - \mathbf{p}_{i,1}}{\|\mathbf{x}_{\text{EPS},i} - \mathbf{p}_{i,1}\|}$ the unit vector pointing to this point, and $\mathbf{e}_{i,2}^{-\perp}$ be a unit vector orthogonal to $\mathbf{e}_{i,2}^-$.

Using these notations a correction is applied on the head node:

$$\mathbf{v}_{\mathbf{e}_{i,1}}^{\text{EPS}} = \gamma (\mathbf{e}_{\text{EPS},i} \cdot \mathbf{e}_{i,2}^{-\perp}) \mathbf{e}_{i,2}^{-\perp},$$

where $\gamma > 0$ models the attraction strength. This velocity tends to change the direction of the head toward the highest concentration of EPS (nematic alignment) with speed γ without changing the value of the speed of the bacterium.

4.2.3. Diversity of bacteria

In experiments on *M. xanthus* (Fig. 1), the length and the width of cells may vary. In SCoPI, we allow bacteria to have a different number of nodes. The description in Sect. 3.3.1 can be easily extended to this case. Similarly, two different bacteria may be modeled with a different radius r . However, we impose that two nodes in the same bacterium have the same radius. In the Python code, bacteria have the same number of nodes with identical radius.

5. NUMERICAL RESULTS

5.1. Contacts dynamics in an unbounded domain

With the modeling framework described previously, we conducted three numerical simulations. Each one incorporates one of the following reversal mechanisms: none, clock-based, and polarity-based. In all three simulations, open boundary conditions are used, that is, cells are not confined to the observed numerical domain

¹Even if a bacterium is isolated, it will have the same number of K detected neighbors as a bacterium surrounded by other cells. However, it will have no effective neighbors in the considered radius r_c and the resulting correction terms exchanged are equal to zero.

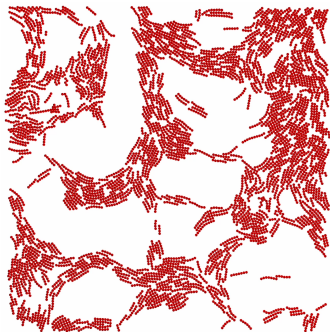


FIGURE 11. Numerical simulation in SCoPI: initial condition.

Parameter	Value
Radius (r)	$0.3 \mu\text{m}$
Cut-off radius (r_c)	$4r$
Velocity of the bacteria (v)	$3 \mu\text{m min}^{-1}$
Overlap between disks (ε)	0
Angle view (2α)	π
Horizon search (H)	$4r$
Stiffness of angular springs (k)	$1 \mu\text{m}^2 \text{min}^{-1}$
Magnitude of the pili attraction (k_a)	$1 \mu\text{m min}^{-1}$
Relative convergence criterion for the Uzawa solver	1×10^{-3}
Step for the gradient descent	2 000

TABLE 1. Numerical parameters used in simulations with SCoPI.

in Fig. 12 and are free to exit. Our first goal is to investigate whether this modeling framework can maintain a swarming pattern if it is initially imposed.

The influence of bending is discussed in [9] and greatly affects the alignment of the cells. In fact, for rigid rods, the outcome of such simulations leads to a global alignment of the bacteria. As shown in Fig. 6 the parameter ε can have a huge impact on the bending of a bacteria. None of these impacts are explored.

5.1.1. Parameters

The three simulations share the following parameters. The initial condition is taken from the experimental data (namely from the frame presented in Fig. 2). The bacteria distribution is identical to a time frame in the live movie where the swarming pattern occurs, see Fig. 11.

The number of disks in a bacterium are inherited from the time frame considered. Values of other parameters are given by Table 1.

5.1.2. Results

In Fig. 12a, we show the final configuration of the simulation at time $t_f = 50 \text{ min}$ in the absence of reversals. Large packs of aligned bacteria are formed and travel together (mainly continuously rotating in the same direction). Isolated bacteria become more scarce throughout the simulation as they join larger groups and travel with them. Interestingly, these patterns were observed in mutant bacteria which have lost the ability to reverse [1].

We then considered initially asynchronous clock-based reversals with a period of $t_f = 1 \text{ min}$, see Fig. 12b. Although open boundary conditions are used allowing bacteria to exit the represented numerical frame, the periodic reversals allow to keep a constant average density. Large packs are able to establish but disintegrate soon after their formation due to the reversals. This result was expected as the reversal mechanism in this case is specific to each bacterium and pertains to its own internal clock, without considering the collective behavior of surrounding bacteria. The swarms are thus unable to form in this case due to the rapid disintegration of packs, allowing for the appearance of isolated bacteria.

Finally, we look at the polarity-based reversal mechanism in Fig. 12c. We notice that we lose the initial bacteria density due to repetitive reversals. The remaining bacteria either travel in large packs or are isolated, and the swarming pattern is lost very fast by the disintegration of packs.

In all three simulations, we notice that the initially imposed swarming pattern is not maintained. The absence of swarming patterns is primarily due to the choice of boundary conditions as we used open boundary conditions to simulate all three scenarios. As a result, the initial given density is lost after some time as bacteria are allowed

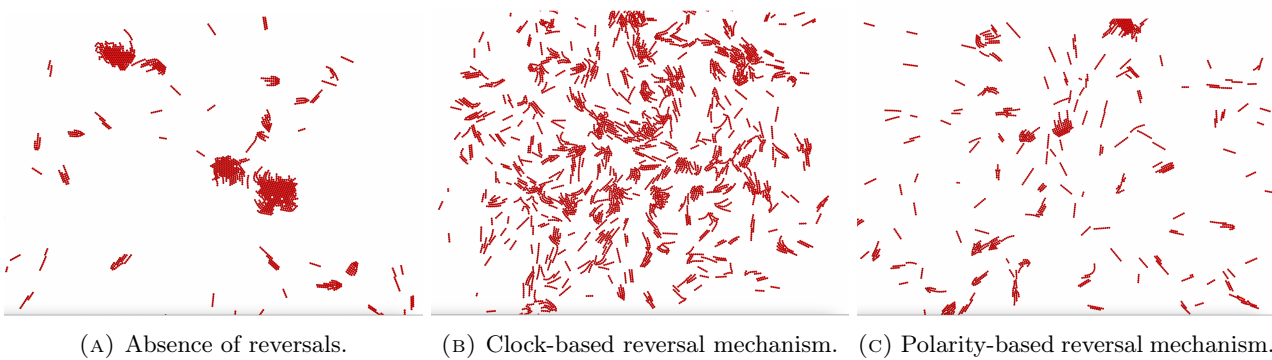


FIGURE 12. Numerical simulation in SCoPI at $t_f = 50$ min.

to exit the observed domain. These simulations clearly suggest a direct link between high congestion and the formation of patterns, as the latter requires the maintenance of congestion (high density in a confined space) to be able to maintain the initially imposed swarms. This is further highlighted in the next section (Sect. 5.2) where we use periodic boundary conditions which confine cells and preserve the initial density.

Altogether, our results recapitulate some behaviors observed in bacteria colonies and reveal the importance of maintaining congestion for the persistence of swarming patterns.

5.2. Velocity-correcting terms with explicit formula and type IV pili

In this section we present the simulations performed with the Python code. We use periodic boundary conditions to keep the bacteria density constant during the entire simulation. We investigate the effect of three features: type IV pili attraction, slime trail following, and polarity-based reversals (defined in Sect. 3.4 and 3.6). We extend the simulation time to 100 min instead of 50 min because the formation of slime trails requires more time to achieve stationary patterns.

All simulations start with a random position and direction for each bacterium (Fig. 13a). Exploring the distinct roles of the features—type IV pili, polarity-based reversal, and slime trail following—we conducted five simulations: one without any feature (Fig. 13b), three testing each feature independently (Figs. 13c to 13e), and one incorporating all three features (Fig. 13f). We use the towed motion (defined in Sect. 3.2) to generate movement, and we do not implement the correction terms defined in Sect. 3.5. This differs from the previous section where the pull motion is used. The model parameters can be found in Table 2.

For the reversals, we employed the last mechanism presented in Sect. 3.4. This mechanism is based on both polarity and the clock, incorporating an implementation of a refractory period—i.e., a duration during which a cell cannot reverse. Figure 13d shows the results when using this reversal feature without any head attraction or slime trail following. In this case, we observe a reduction in the size of the group compared to the simulation without features (Fig. 13b), consistent with the results presented in Balagam et al. [1].

The attraction due to the action of the pili does not seem to exhibit a significant difference when compared with the simulation without features (compare Fig. 13c and Fig. 13b). There might be only an effect on the size of the groups and on the number of isolated bacteria, although this should be confirmed through a more in-depth analysis.

The slime trail following confines each bacterium within the most explored space. After 100 min of simulation, Fig. 13e reveals a significant portion of bacteria following a lengthy trail on the left side of the simulation. Additionally, the simulation illustrates a substantial gathering of bacteria in the upper right, forming new slime areas. In the first scenario, bacteria align along the long EPS road, while in the second scenario, the absence of well-defined EPS roads results in steric constraints outweighing the EPS constraints. This leads to a group primarily constrained by steric factors rather than EPS, allowing cells to escape from the slime trail and create new slime areas.

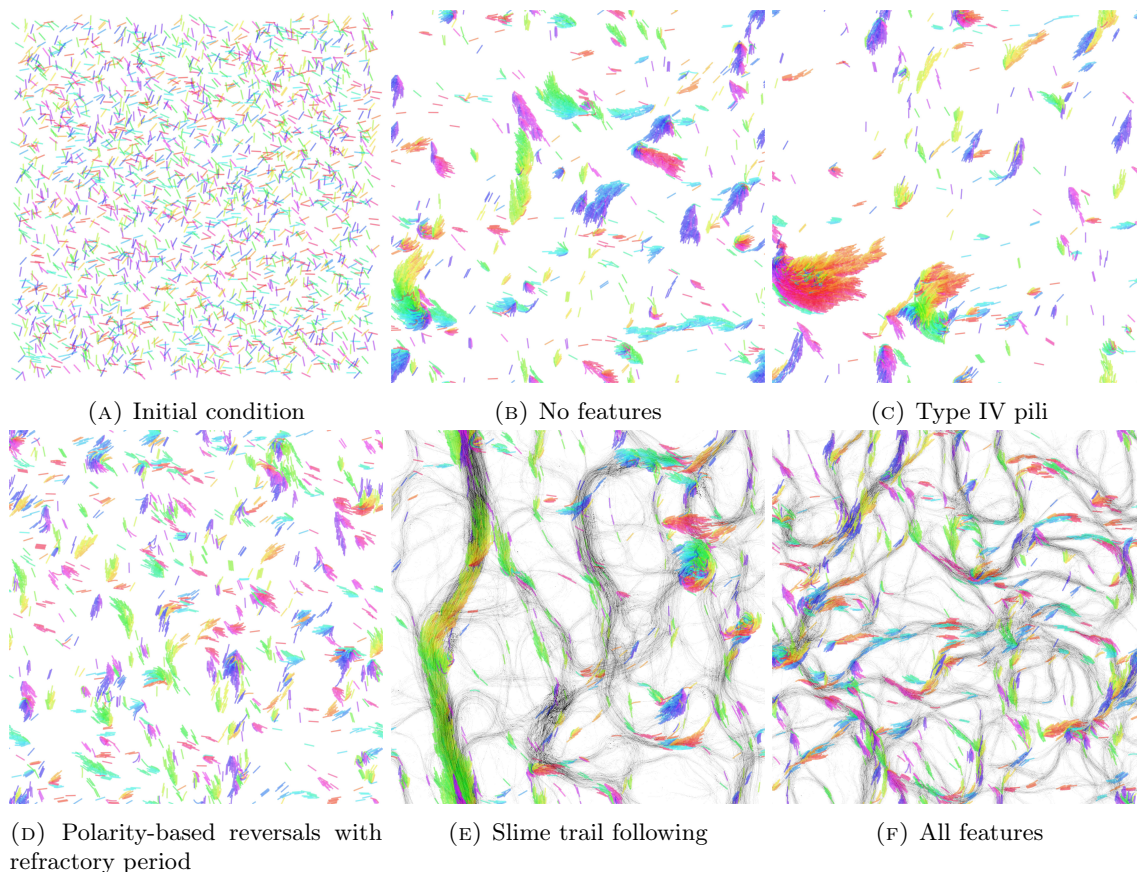
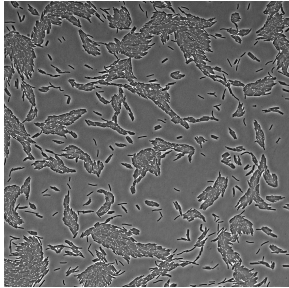


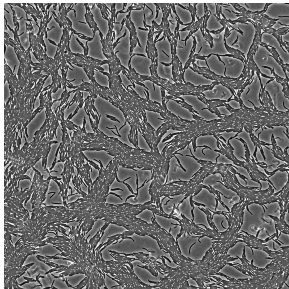
FIGURE 13. Results of the numerical simulations in Python after 100 min. Bacteria are colored depending on the direction of their head.

The combination of all features is depicted in Fig. 13f. Bacteria are trapped in the slime trails, and the polarity-based reversals prevent the formation of large groups that might cease to be constrained by the EPS due to steric contact, as shown in Fig. 13e. When a group becomes too large and meets another group, many cells can reverse due to the increased polarity signal. These reversals respond to the congestion of the cells, dividing the groups into smaller ones and preventing the formation of large groups, as observed in Fig. 13d. The effect of pili attraction, as seen in Fig. 13c, is also unclear in this context. This falls within the scope of the sensitivity analysis of model parameters, which we keep for future work. In conclusion, this simulation reveals a greater diversity of bacteria trails compared to Fig. 13e.

In Fig. 14, we can see two different patterns of swarming of *M. xanthus* observed in experiments. The left panel of the figure shows patterns that are similar to those observed in Figs. 13b and 13c. In fact, the simulation with polarity-based reversal only, represented by the Fig. 13d, seems to exhibit smaller group organization. The simulation recapitulates very well the cell behavior in the experimental data where cells explore all the space uniformly over time. The right panel, in which certain areas are never visited (simulation video not included in the data shown here), shows similar behavior to what we observe in Fig. 13f with the slime trail following feature. These patterns arise from the observation of *M. xanthus* colonies, but the specific conditions that give rise to such patterns are currently unknown.



(A) Cell pattern leaving no empty spaces.



(B) Cell pattern leaving empty spaces.

FIGURE 14. Phase contrast images of the *M. xanthus* colony taken with $100\times$ magnification objective.

Parameter	Value
Size of the space	195 μm
Number of bacteria (M)	2 700
Number of disks per bacterium (N)	10
Radius of the disks (r)	0.3 μm
Velocity of the bacteria (v)	3 $\mu\text{m min}^{-1}$
Overlap between disks (ε)	0.1 μm
Hooke's spring constant (k_s)	50 min^{-1}
Repulsion coefficient (k_r)	400 $\mu\text{m}^{-1} \text{min}^{-1}$
Angle view (2α)	π
Horizon search (H)	$4r = 1.2 \mu\text{m}$
Magnitude of the pili attraction (k_a)	1 $\mu\text{m min}^{-1}$
EPS attraction strength (γ)	6 $\mu\text{m min}^{-1}$
EPS evaporation rate (λ)	$\frac{1}{12} \text{min}^{-1}$
Minimal EPS value detectable (c_{min})	0.1
Refractory time (t_{ref})	5 min
Willingness to reverse (w)	3

TABLE 2. Numerical parameters used in simulations with Python.

6. DISCUSSION AND CONCLUSION

In this paper, we presented two mathematical models in the spirit of [1]. The main novelty is the polarity-based reversal mechanism of *M. xanthus* bacteria. We brought to light this mechanism using image and data analysis of biological experiments on *M. xanthus* bacteria. The first model follows a contact dynamics approach. It is implemented using the SCoPI code. The second model treats cell-cell contacts with attractive-repulsive distance-dependent velocity-correcting terms with an explicit formulation. This model is implemented in Python and is additionally endowed with the slime trail following mechanism. Let us notice that the implementation of the slime trail following model was not achieved in SCoPI due to time constraints and is left for future works. For the same reason the stiffness model discussed in Sect. 3.5 is only implemented in SCoPI. Our numerical simulations with SCoPI first reveal the importance of appropriate boundary conditions in the contact dynamics approach. Considering periodic boundary conditions will keep the initial density constant throughout the numerical simulations, which allows for constant high congestion. Using periodic boundary conditions show the persistence of cell congestion. The drawback of using explicit formulation for the velocity-correcting terms is the necessity to fine-tune the attractive-repulsive forces to be able to reproduce the observed dynamics. This tuning is rather difficult as the experimental data on hand do not allow us to do so. On the other hand, although the cell motility mechanisms are sufficient to reproduce the bacteria motility observed in the experimental data, both models could make use of combining different motility mechanisms. For example, we could endow the bacteria with the ability to alternate its motility between the towed and the pulled motilities depending on its environment. This is motivated by the fact that in the presence of neighboring bacteria, the pili are the main drivers of cell motility (towed), whereas when isolated, cells move using the pulled mechanism on the substrate. In a future work, we want to implement the EPS deposit and run simulations using periodic boundary conditions with SCoPI.

Overall, our image analysis as well as our numerical simulations reveal a novel reversal mechanism to the literature based on cell polarity, which can explain the emerging patterns at the colony level.

REFERENCES

- [1] Rajesh Balagam and Oleg A Igoshin. Mechanism for collective cell alignment in myxococcus xanthus bacteria. *PLoS computational biology*, 11(8):e1004474, 2015.
- [2] Jose Luis Blanco and Pranjal Kumar Rai. nanoflann: a C++ header-only fork of FLANN, a library for nearest neighbor (NN) with kd-trees. <https://github.com/jlblancon/nanoflann>, 2014.
- [3] P.A. Cundall and O.D.L. Strack. A discrete numerical model for granular assemblies. *Géotechnique*, 29(1):47–65, 1979. Publisher: ICE Publishing.
- [4] Pierre Degond, Angelika Manhart, and Hui Yu. An age-structured continuum model for myxobacteria. *Mathematical Models and Methods in Applied Sciences*, 28(09):1737–1770, 2018.
- [5] Mathilde Guzzo, Seán M Murray, Eugénie Martineau, Sébastien Lhospice, Grégory Baronian, Laetitia My, Yong Zhang, Leon Espinosa, Renaud Vincentelli, Benjamin P Bratton, et al. A gated relaxation oscillator mediated by frzx controls morphogenetic movements in myxococcus xanthus. *Nature microbiology*, 3(8):948–959, 2018.
- [6] Oleg A Igoshin, Alex Mogilner, Roy D Welch, Dale Kaiser, and George Oster. Pattern formation and traveling waves in myxobacteria: theory and modeling. *Proceedings of the National Academy of Sciences*, 98(26):14913–14918, 2001.
- [7] Mourad Ismail and Aline Lefebvre-Lepot. A Necklace Model for Vesicles Simulations in 2D. *International Journal for Numerical Methods in Fluids*, 76(11):835–854, December 2014.
- [8] Albertas Janulevicius, Mark CM van Loosdrecht, Angelo Simone, and Cristian Picioreanu. Cell flexibility affects the alignment of model myxobacteria. *Biophysical journal*, 99(10):3129–3138, 2010.
- [9] Albertas Janulevicius, Mark C.M. Van Loosdrecht, Angelo Simone, and Cristian Picioreanu. Cell Flexibility Affects the Alignment of Model Myxobacteria. *Biophysical Journal*, 99(10):3129–3138, November 2010.
- [10] M. Jean. The non-smooth contact dynamics method. *Computer Methods in Applied Mechanics and Engineering*, 177(3):235–257, 1999.
- [11] M. Jean and J. J. Moreau. Unilaterality and dry friction in the dynamics of rigid body collections. In *1st Contact Mechanics International Symposium*, pages 31–48, Lausanne, Switzerland, 1992.
- [12] Lars Jelsbak and Lotte Søgaard-Andersen. Pattern formation: fruiting body morphogenesis in myxococcus xanthus. *Current Opinion in Microbiology*, 3(6):637–642, 2000.
- [13] Aline Lefebvre. Numerical simulation of gluey particles. *ESAIM: Mathematical Modelling and Numerical Analysis - Modélisation Mathématique et Analyse Numérique*, 43(1):53–80, 2009.
- [14] A. Lefebvre-Lepot. SCoPIwebpage, <http://www.cmap.polytechnique.fr/~lefebvre/SCoPI/index.html>, 2022.
- [15] Yinuo Li, Hong Sun, Xiaoyuan Ma, Ann Lu, Renate Lux, David Zusman, and Wenyuan Shi. Extracellular polysaccharides mediate pilus retraction during social motility of myxococcus xanthus. *Proceedings of the National Academy of Sciences*, 100(9):5443–5448, 2003.
- [16] Angelika Manhart. Counter-propagating waves in a system of transport-reaction equations. *arXiv preprint arXiv:1801.06869*, 2018.
- [17] H. Mazhar, T. Heyn, D. Negrut, and A. Tasora. Using nesterov’s method to accelerate multibody dynamics with friction and contact. *ACM Transactions on Graphics (TOG)*, 34(3):1–14, 2015.
- [18] T Mignot. The elusive engine in myxococcus xanthus gliding motility. *Cellular and Molecular Life Sciences*, 64:2733–2745, 2007.
- [19] Tãm Mignot, Joshua W Shaevitz, Patricia L Hartzell, and David R Zusman. Evidence that focal adhesion complexes power bacterial gliding motility. *Science*, 315(5813):853–856, 2007.
- [20] J.J. Moreau. Unilateral Contact and Dry Friction in Finite Freedom Dynamics. In J.J. Moreau and P.D. Panagiotopoulos, editors, *Nonsmooth Mechanics and Applications*, International Centre for Mechanical Sciences, pages 1–82. Springer, Vienna, 1988.
- [21] J.J. Moreau. Numerical aspects of the sweeping process. *Computer Methods in Applied Mechanics and Engineering*, 177(3-4):329–349, 1999.
- [22] Swapnesh Panigrahi, Dorothée Murat, Antoine Le Gall, Eugénie Martineau, Kelly Goldlust, Jean-Bernard Fiche, Sara Rombouts, Marcelo Nöllmann, Leon Espinosa, and Tãm Mignot. Mistic, a general deep learning-based method for the high-throughput cell segmentation of complex bacterial communities. *eLife*, 10:e65151, sep 2021.
- [23] M. A. Peletier. Variational modelling: Energies, gradient flows, and large deviations. Lecture Notes, Würzburg. Available at <http://www.win.tue.nl/~mpeletie>, Feb. 2014.
- [24] Brian Sager and Dale Kaiser. Intercellular c-signaling and the traveling waves of myxococcus. *Genes & Development*, 8(23):2793–2804, 1994.
- [25] Hale F Trotter. On the product of semi-groups of operators. *Proceedings of the American Mathematical Society*, 10(4):545–551, 1959.

- [26] Katherine G Trudeau, Mandy J Ward, and David R Zusman. Identification and characterization of frzz, a novel response regulator necessary for swarming and fruiting-body formation in myxococcus xanthus. *Molecular microbiology*, 20(3):645–655, 1996.
- [27] Takagi Tsutomu, Moritomi Yutaka, Iwata Jyun, and Nakamine Hiroshi. Mathematical model of fish schooling behaviour in a set-net. *Journal of Marine Science*, 61(7):1054–3139, 2004.
- [28] Jorge Velázquez-Castro, Milica Lakovic, Esli Morales-Tehuitzil, Inti A. Pagnuco, Carmen A. Ramírez, and Raul Costa-Pereira. A mathematical model of anarchy in bees. *Apidologie*, 51(6):1117–1124, 2020.
- [29] Tamás Vicsek, András Czirók, Eshel Ben-Jacob, Inon Cohen, and Ofer Shochet. Novel type of phase transition in a system of self-driven particles. *Phys. Rev. Lett.*, 75(6):1226–1229, Aug 1995.
- [30] Tamás Vicsek and Anna Zafeiris. Collective motion. *Physics Reports*, 517(3):71–140, 2012.
- [31] Yong Zhang, Adrien Ducret, Joshua Shaevitz, and Tãm Mignot. From individual cell motility to collective behaviors: insights from a prokaryote, myxococcus xanthus. *FEMS microbiology reviews*, 36(1):149–164, 2012.

A. A GRADIENT-FLOW MODEL FOR THE STIFFNESS OF A BACTERIUM

As explained in Sect. 3.5, the usual model of stiffness does not preserve intercenter distances. This can be clearly seen in Figs. 15a to 15c for a three-disk long bacterium.

To remedy this issue, we derive an L^2 gradient-flow of the discrete curvature energy: $\sum_j \frac{\|\mathbf{e}_{i,j}^+ + \mathbf{e}_{i,j}^-\|^2}{2R}$ associated with the constraint $d_{i,j}^{i,j\pm 1} = -\varepsilon$ [23]. To compare the models, we provide explicit computations for a three-disk long bacterium (Figs. 15d to 15f). The derivative of the energy with respect to the position, and therefore the velocity-correcting terms (up to a negative multiplicative constant $-C$) is:

$$\begin{pmatrix} \frac{d}{dt} \mathbf{p}_{i,1} \\ \frac{d}{dt} \mathbf{p}_{i,2} \\ \frac{d}{dt} \mathbf{p}_{i,3} \end{pmatrix} = -C \begin{pmatrix} 2(\mathbf{e}_{i,2}^+ + \mathbf{e}_{i,2}^-) + \pi_{1,2} \mathbf{e}_{i,2}^- \\ -4(\mathbf{e}_{i,2}^+ + \mathbf{e}_{i,2}^-) - \pi_{1,2} \mathbf{e}_{i,2}^- - \pi_{3,2} \mathbf{e}_{i,2}^+ \\ 2(\mathbf{e}_{i,2}^+ + \mathbf{e}_{i,2}^-) + \pi_{3,2} \mathbf{e}_{i,2}^+ \end{pmatrix} \quad (6)$$

where $\pi_{1,2}$ and $\pi_{3,2}$ are the Lagrange multiplier associated with the constraints $d_{i,1}^{i,2} = -\varepsilon$ and $d_{i,3}^{i,2} = -\varepsilon$, respectively. To find the values of $\pi_{1,2}$ and $\pi_{3,2}$, we compute the time derivative of the square of the two constraint equations $d_{i,1}^{i,2} = -\varepsilon$ and $d_{i,2}^{i,3} = \varepsilon$:

$$\begin{cases} \left(\frac{d}{dt} \mathbf{p}_{i,1} - \frac{d}{dt} \mathbf{p}_{i,2} \right) \cdot \mathbf{e}_{i,2}^- = 0 \\ \left(\frac{d}{dt} \mathbf{p}_{i,3} - \frac{d}{dt} \mathbf{p}_{i,2} \right) \cdot \mathbf{e}_{i,2}^+ = 0. \end{cases} \quad (7)$$

As Eq. (7) is a linear combination of Eq. (6), we can compute $\pi_{1,2}$ and $\pi_{3,2}$ as

$$\pi_{1,2} = \pi_{3,2} = -6 \frac{\mathbf{e}_{i,2}^+ \cdot \mathbf{e}_{i,2}^- + 1}{\mathbf{e}_{i,2}^+ \cdot \mathbf{e}_{i,2}^- + 2}.$$

We still have to fix the proportionality constant that links the derivative of the energy and the velocity-correcting terms. We choose it such that this model behaves as the model described in Sect. 3.5 for shallow angles:

$$\begin{aligned} \mathbf{v}_{\mathbf{e}_{i,1}}^{i,2} &= -\frac{k}{R} \left(\mathbf{e}_{i,2}^+ - \frac{2\mathbf{e}_{i,2}^+ \cdot \mathbf{e}_{i,2}^- + 1}{\mathbf{e}_{i,2}^+ \cdot \mathbf{e}_{i,2}^- + 2} \mathbf{e}_{i,2}^- \right) \\ \mathbf{v}_{\mathbf{e}_{i,3}}^{i,2} &= -\frac{k}{R} \left(\mathbf{e}_{i,2}^- - \frac{2\mathbf{e}_{i,2}^+ \cdot \mathbf{e}_{i,2}^- + 1}{\mathbf{e}_{i,2}^+ \cdot \mathbf{e}_{i,2}^- + 2} \mathbf{e}_{i,2}^+ \right) \\ \mathbf{v}_{\mathbf{e}_{i,2}}^{i,2} &= -\mathbf{v}_{\mathbf{e}_{i,1}}^{i,2} - \mathbf{v}_{\mathbf{e}_{i,3}}^{i,2}. \end{aligned}$$

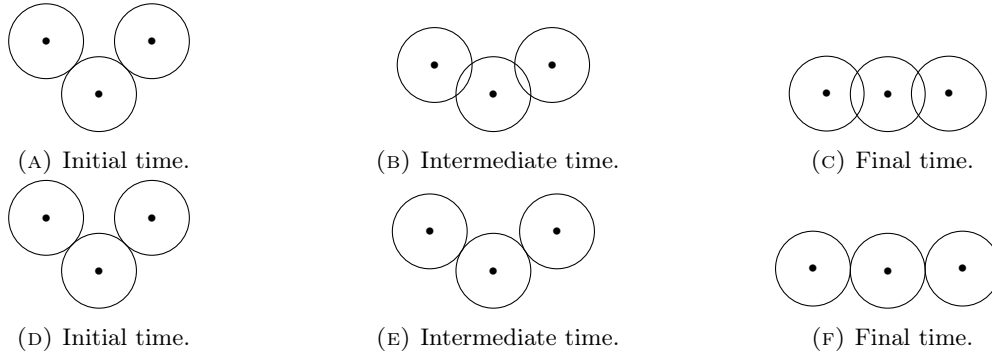


FIGURE 15. Stiffness-driven evolution of a three-disk bacterium. Top, angular springs model. Bottom, gradient flow-model.

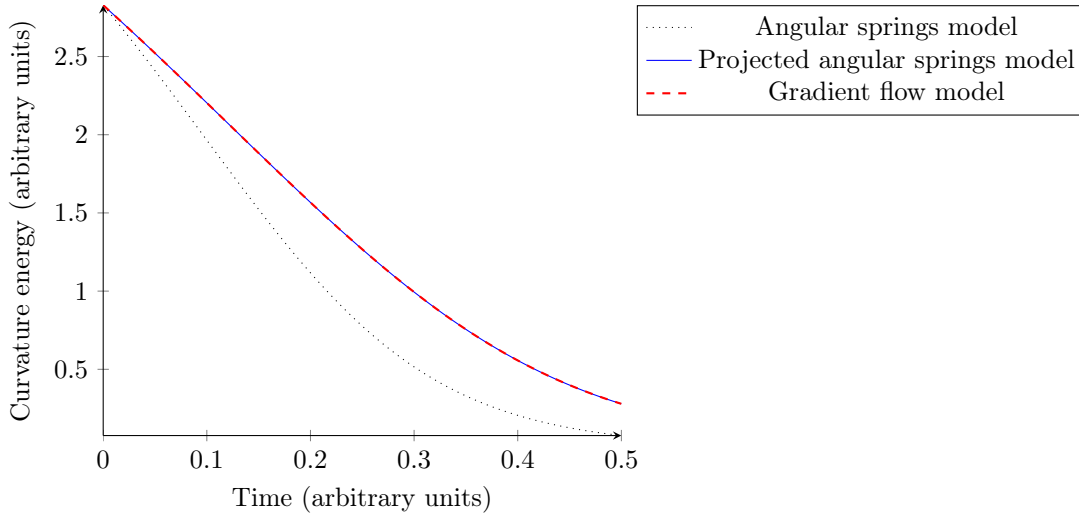


FIGURE 16. Evolution of curvature energy with time.

Although the gradient-flow model has interesting properties, its implementation is tedious since it requires explicit computations for each length of bacteria N in the simulation. As can be noticed in Table 1, N is not defined. Indeed, since the length of the bacteria is based on realistic data, we have several bacterium sizes. To get the velocity-correcting terms, we have to inverse a linear systems for each value of N , which can be costly.

Another point in favor of Eq. (3) is that we can derive the gradient flow model from the usual model. Indeed, the implicit contact velocity-correcting terms defined in Sect. 3.3.1 can be seen as the smallest (in L^2) perturbation of the correction given by the first model that satisfies the constraint. Using the orthogonality in the optimization formulation of the gradient flow, we notice that that for bacteria that do not cross themselves we obtain the gradient-flow model. This is emphasized by Fig. 16. For the sake of simplicity and due to the independent implementation of contact forces, we only consider Eq. (3) when accounting for the stiffness. Notice that due to the implementation of other forces the gradient flow and usual implementation of the stiffness would give slightly different models even when using Sect. 3.3.1.

This model was not used in the simulations described in Sect. 5.